Optically Quantifying Spatiotemporal Responses of Water Injection-Induced Strain via Downhole Distributed Fiber Optics Sensing

Yankun Sun[1,1], Ziqiu Xue[1,1], Tsutomu Hashimoto[1,1], and Yi Zhang[1,1]

[1]Research Institute of Innovative Technology for the Earth

November 30, 2022

Abstract

Harsh subsurface environment limits robust workability of on-site instrumentation to be leveraged to track solid Earth's dynamics. Distributed fiber-optic sensing technology (DFOS) allows long-period in-situ real-time detection of crustal geoenergy exploration-induced underground motions. Here, we first deployed 300-m-long fiber-optic cables behind casing of an actual injection well via single-ended, hybrid Brillouin-Rayleigh backscatterings interrogator to distributed monitor water injection test between two adjacent wells in onshore Mobara, Japan. Detailed DFOS recordings over the entire borehole visualized clear-cut spatiotemporal strain responses from one water injection. Potential injected water-transport footprint and impacted zone reasonably coincided with those of analogy-based strain fronts. Our study thus further uncovered that injection volume and injection pressure significantly dominated water injection-driven strain magnitude and coverage.

1

Optically Quantifying Spatiotemporal Responses of Water Injection-Induced Strain via Downhole Distributed Fiber Optics Sensing

Yankun Sun[1, 2], Ziqiu Xue[1, 2], Tsutomu Hashimoto[1, 2], Yi Zhang[1, 2]

[1]Geological Carbon Dioxide Storage Technology Research Association, 9-2 Kizugawadai, Kizugawa-shi, Kyoto

619-0292, Japan

[2]Research Institute of Innovative Technology for the Earth, 9-2 Kizugawadai, Kizugawa-shi, Kyoto 619-0292, Japan

Corresponding author: Yankun Sun, sun@rite.or.jp.

Key Points:

• Novel hybrid fiber optics is exploited to distributed monitor strain responses along a 300-m borehole in a fibered injection well.

• Clear-cut spatiotemporal strain profiles/fronts in one water injection section have been captured via one single sensor cable.

• Combined effects of injection scenario on injection-induced strain are first explored quantitatively.

Abstract

Harsh subsurface environment limits robust workability of on-site instrumentation to be leveraged to track solid Earth's dynamics. Distributed fiber-optic sensing technology (DFOS) allows long-period in-situ real-time detection of crustal geoenergy exploration-induced underground motions. Here, we first deployed 300-m-long fiber-optic cables

behind casing of an actual injection well via single-ended, hybrid Brillouin-Rayleigh

backscatterings interrogator to distributed monitor water injection test between two

adjacent wells in onshore Mobara, Japan. Detailed DFOS recordings over the entire

borehole visualized clear-cut spatiotemporal strain responses from one water injection.

Potential injected water-transport footprint and impacted zone reasonably coincided

with those of analogy-based strain fronts. Our study thus further uncovered that

injection volume and injection pressure significantly dominated water injection-driven

strain magnitude and coverage.

Plain Language Summary

Distributed fiber optic sensing is an emerging technique to monitor dense geophysical

information inside the Earth. This study explores in greater detail spatiotemporal strain

evolutions from one water injection process in an actual 300-m-deep well via FO cables

based on hybrid Brillouin-Rayleigh backscatterings at unprecedented resolution. Clear-

cut strain profiles portray water migration footprints, and observed strain fronts are

good agreement with impacted extent. Measurable strain magnitude and evolutions

closely depend on injection scenario. These findings open up a new avenue for finely

optical geoenergy monitoring and fluid evolution imaging that boost all-optical

early-warning potential and quantitative risk decision-making for future quasi-geodetic

strain-related geohazards.

1. Introduction

40   Massive fluids injection and/or production such as CO_2 geological storage (CGS) and

41   groundwater withdrawal often pose pore pressure perturbation, ultimately resulting in

42   near-surface geomechanical deformation (i.e., strain): ground uplift or subsidence.

43   Moreover, fluid injection-induced deformation can potentially create or reactivate

44   fractures and faults in reservoir-caprock systems, thereby triggering unfavorable

45   leakage pathways or microseismic/felt-earthquake occurrence (Baatz et al., 2015;

46   White et al., 2014; Zoback and Gorelick, 2012). Monitoring in-situ deformation/strain

47   distributions from injection reservoirs to surface is thus important to obtain a complete

48   understanding of crustal geomechanics in various near-surface geoengineerings.

49   Typical strain-recording instruments utilized in various CGS sites mainly include global

50   positioning system (GPS) (Karegar et al., 2015; McColpin, 2009), interferometric

51   synthetic aperture radar (InSAR) (Ferretti et al., 2011; Vasco et al., 2010), tiltmeter

52   (Murdoch et al., 2019; Siriwardane et al., 2013), seismic/microseismic geophones (Arts

53   et al., 2004; Chadwick et al., 2004; Saito et al., 2006; Verdon et al., 2015). However,

54   these instrumentations possess low resolution, small coverage, high cost, discrete

55   detection, time-consuming, short term, poor signal-to-noise ratio (SNR), etc. (Verdon et

56   al., 2013), apart from subsurface complexity, limiting us to refine images of deep

57   reservoir geomechanical responses (Jousset et al., 2018). Hence full- depth strain

58   profiles regarding precisely how the near-wellbore strata deform vertically at higher

59   spatial and temporal resolution in CO_2 storage environments are unclear. Despite

60   efforts aimed at developing CGS-related downhole sensors, some challenges remain

61   poorly addressed, including high-pressure high-temperature (HPHT), stronger

62   corrosivity, indirect and point detection, etc. (Arts and Vandeweijer, 2011; Baldwin,

63   2014b; Shanafield et al., 2018).

64   Distributed fiber-optic sensing (DFOS) technologies, an emerging technology that turns

65   optical fiber into an array of sensors, allows for densely distributed strain measurement

66   along a single fiber optic (FO) cable (Bao and Chen, 2012; Kogure and Okuda, 2018;

67   Miah and Potter, 2017). One major benefit of DFOS is that it can record the

68   measurands (e.g., temperature, strain, pressure, vibration and acoustics) as a function

69   of the position along the entire FO length (Schenato, 2017). Distributed temperature

70   sensing (DTS) with Raman scattering, Brillouin/Rayleigh scattering-based distributed

71   strain sensing (DSS) and distributed acoustic sensing (DAS) with Rayleigh scattering are

72   the most frequently-used DFOS in the oil and gas industry for many decades (Kersey,

73   2000). However, only a few studies have explored DFOS potential for downhole sensing

74   applications (Bense et al., 2016; Karrenbach et al., 2017; Lellouch et al., 2019).

75   Recently, DFOS has been introduced to monitor CGS-related small strains in laboratory

76   and field tests. Zhang et al., (2019) and Zhang and Xue (2019) observed CO_2 plume or

77   brine migration behaviors in a Tako sandstone core via Rayleigh-based DFOS and X-ray

78   computed tomography. Lei et al., (2019) and Xue et al., (2018) deployed three FO

79   cables behind casing to sense strain responses from pumping water in two neighboring

80   wells. Sun et al., (2019) measured in-situ strain distributions induced by water injection

81   tests performed in a well close to the fibered well. These lab-field investigations push

82   DFOS technique to densely apply in geoscience monitoring fields.

83   In this Letter we implement in-depth analyses for spatiotemporal strain profiles using

84   DFOS with hybrid Brillouin-Rayleigh scattering in one water injection field test analogy

85   to CGS process. We find that (1) strain magnitude and patterns are associated with

86   injection scenario, and (2) potential injected water-transport footprint and affected

87   regions coincide with those of analogy-based strain fronts. We show that downhole

88   DFOS can provide new insights into imaging Earth's dynamics with unprecedented

89   levels of detail, illuminating future farfield multi-well strain monitoring for large-scale

90   long-term CGS projects.

91   ## 2. Methodology

92   ### 2.1. DFOS Principle with Hybrid Brillouin-Rayleigh Scattering

93   Downhole DFOS can monitor the entire surface-bottom profile that is impossible with

94   point sensors or even wireline tools. Another is that glass fiber by its nature is immune

95   to electromagnetic interference (Sun et al., 2018), can transmit data at high speeds,

96   and can operate in extreme environments. All of these attributes make DFOS a robust

97   solution for real-time long-distance in-situ life-of-well measurements.

98   Novel DFOS technology in this study is integrating Brillouin and Rayleigh backscattering

99   into only one single-mode (SM) optical fiber (Figures 1 and S1A). It consists of synthetic

100   Brillouin optical time domain reflectometry (S-BOTDR) and tunable wavelength

101   coherent optical time domain reflectometry (TW-COTDR), allowing SM fiber to

102   simultaneously monitor strain and temperature along the fiber (Kishida et al., 2012).

103   Here, S-BOTDR can achieve 10- cm spatial resolution (Nishiguchi et al., 2014) and

104   TW-COTDR processing the same sensitivity as a conventional fiber Bragg grating sensor,

105   is especially well-suited to detect small temperature and/or strain changes. (Wu et al.,

106   2016). This hybrid system has their both advantages with higher spatial resolution of 5

107   cm than that of 1 m for other sensors.

108   S-BOTDR is based on single-ended spontaneous Brillouin scattering. Incident light will

109   interact with acoustic phonons induced by thermal fluctuation or applied strain onto

110   an optical fiber. Backscattered light has a Doppler shift (i.e., Brillouin frequency shift) in

111   proportion to strain or temperature changes along the FO cable. Brillouin frequency

112   shift, denoted as Δv_B, can be expressed as

113
$$\Delta v_B = \frac{\partial v_B}{\partial \varepsilon} \Delta \varepsilon + \frac{\partial v_B}{\partial T} \Delta T \qquad (1)$$

114   where $\Delta \varepsilon$, ΔT, $\partial v_B / \partial \varepsilon$, $\partial v_B / \partial T$ are the strain and temperature increments, strain

115   and temperature coefficients in Brillouin sensing, respectively.

116   TW-COTDR is based on single-ended time domain Rayleigh scattering. Power spectrum

117   in TW-COTDR will occur due to refractive index fluctuations with random heterogeneity

118   of glass density in the fiber core (Froggatt & Moore, 1998). Rayleigh frequency shift is

119   obtained by comparing the measured value in reference state via cross-correlation

120   (Kishida et al., 2012). The frequency shift Δv_R induced by strain/temperature changes

121 can be depicted using the linear equation:

$$\Delta v_R = \frac{\partial v_R}{\partial \varepsilon} \Delta \varepsilon + \frac{\partial v_R}{\partial T} \Delta T \qquad (2)$$

123 where $\Delta\varepsilon$, ΔT, $\partial v_R/\partial \varepsilon$, $\partial v_R/\partial T$ are the strain and temperature increments, strain

124 and temperature coefficients in Rayleigh sensing, respectively.

125 Hybrid Brillouin-Rayleigh system can measure a separated temperature and strain using

126 a single SM fiber by simultaneously solving Eqs. 1 and 2. For field monitoring for water

127 injection via FO cables, a NeubreScope NBX-8000 optical interrogator (Neubrex Co.,

128 Kobe, Japan) was employed (Figure S1B). The sampling resolution and spatial

129 resolution were set to 5 cm and 10 cm, respectively; the hybrid measurement accuracy

130 was 10 με/0.5℃ over a long distance (~25 km) (Table S1). The strain and temperature

131 coefficients for Rayleigh frequency shift from one-layer armored cable used in this field

132 site were determined experimentally to -0.1535 GHz/με and -3.372 GHz/°C (Table S2).

133 **2.2. Fiber Optic Cable Deployment and Water Injection Procedure**

134 Three different types of FO cables were deployed behind casing of 300-m fibered well

135 in Mobara, Chiba Perf., Japan (Figure 1A). Cable specifications and sensing modes are

136 detailed in Sun et al., (2020) and Table S3. The FO cables ran from optical interrogator,

137 which was set in a house near the testing site, in turn crossed bellows, underground

138 horizontal polyvinyl chloride (PVC) pipes, bellows and external casing up to the 295-m-

139 deep bottomhole (Figure 1B). These cables were single-end coupled well with external

140 casing using specialized coupling protectors, fiber clamps and cable centralizers. Cables

141 were cemented within the annulus between casing and formation along the entire well

142 depth; thereby full-bore monitoring strain variations can be realized. Note that all

143 strains presented in this letter are vertical and relative strains recorded by one-layer

144 armored cable (1A) via TW-COTDR sensing. Although Brillouin data were collected with

145 S-BOTDR in these field tests, the main reason why they were not shown in this study is

146 higher resolution and higher SNR of Rayleigh sensing than that of Brillouin sensing,

147 which was concurrently logged to remove the strain and temperature cross-sensitivity

148 effects with a single BrugSteel (Brugg Cables, Switzerland) FO cable (Sun et al., 2020).

149
> **Insert Figure 1 here.**

150 Field water injection test was implemented between two adjacent vertical wells (5.5 m

151 apart) with depths of 230 m and 300 m (Figure 1C). A 230-m-deep well acting as an

152 injection well (IW #2) was drilled subsequent to 300-m-deep fibered monitoring well

153 (MW #1). The whole geological section of MW #1 is described in Table S4. Water was

154 injected through perforating fractures in IW #2 into targeted sand layers linking both

155 wells, and gradually migrated to the fibered well, thus aiming to sense resulting strain

156 responses via previously installed cables. Moreover, injection pressure and injection

157 temperature were measured using pressure/temperature (P/T) sensors built into the

158 drill pipe near the injection ports in IW #2 (Figure 1C).

159 Prior to water injection, borehole cementing and temperature equilibration were last

160 for 25 days. Two injection tests were performed (Table S5). Additionally,

161 multi-instrument logging including electrical micro imager (EMI), radial cement bond

162 log (RCBL), ultrasonic and radioactive logging were exploited conjointly with downhole

163 DFOS monitoring in MW #1.

3. Results

3.1. In-Depth Analyses of Water Injection Scenario

166 During the whole injection process, injection rate was collected by wellhead flowmeter;

167 injection pressure and injection temperature were acquired simultaneously employing

168 P/T sensors installed in the borehole at 187.8 m depth in IW #2. Preinjected water was

169 prepared in the storage tank with temperature of approximately 10 °C. Figure 2 shows

170 detailed relationships between water injection scenarios with induced strain changes

171 and provides new insights regarding how injection behavior affects interwell strain.

172 Based on the injection rate (Figure 2A), water injection test comprised six stages:

173 pre-injection (**I**), low flowrate injection (**II**) with 12 L/min, unplanned stop (**III**), high

174 flowrate injection (**IV**) with 120 L/min, moderate flowrate injection (**V**) with 80 L/min

175 and post-injection (**VI**). At early stage (before 10:32), there was insignificant effect of

176 injection pattern on the vertical strain, while for mid-late stage, injection water volume

177 had a similar increasing pace with three strain profiles, indicating that cumulative mass

178 was dominant effect.

179 Measurable frequency shifts resulted from changes in strain and temperature. Hence,

180 in this study, water temperature was measured in IW borehole and via FIMT in MW #1.

181 Injection temperature varied from 16.5℃ to 12.9℃ with maximum difference of 3.6℃

182 (Figure 2B) as well as maximum temperature increment of 0.02℃ monitored by FIMT

183 (Figure S4). Hence, although injection temperature changed relatively notable in IW,

184 observed temperature increment in MW was so small that its effect could be negligible,

185 mainly due to temperature equilibrium of migrating water between 5.5-m intervals.

186
<div style="text-align:center;">

Insert Figure 2 here.

</div>

187 Fluid pressure highly alters the reservoir-caprock geomechanics around the wellbore

188 and largely reflects formation injectivity. Figure 2C shows details of injection pressure

189 fluctuations and corresponding strain responses. Once injection was started, pressure

190 variation constrained about 0.2 MPa and initial strain behave negative, implying that

191 the formation experienced compressive deformation. With pressure increasing (i. e., **IV**

192 stage), pressure increment rose to 0.5 MPa corresponding to +43 με strain @187.8 m

193 along with maximum pressure gradient of 210 MPa/s, This situation was also applicable

194 to post-injection with decreasing pressure. However, when injection pressure remained

195 relatively stable, approximately 2.1 MPa accompanying ΔP=0.4 MPa and dP/dt=0

196 MPa/s (as marked with horizontal gray dashed line in Figure 2C), injection pressure had

197 minimal influence on strain changes for this phase (**IV** and **V**). In addition, there were

198 two notable leaps of pressure gradient occurred at 10:15 and 14:05, where strains just

199 changed dramatically. This is the first time to quantify how injection scenario affected

200 injection-induced strain. Thus, these findings further reveal that injection scenario

201 plays a critical role in dominating water injection-driven strain magnitude and status

3.2. Finely Quantifying Spatiotemporal Strain Evolutions

S-BOTDR signal acted as reference for strain and temperature separation, TW-COTDR

data sampled every 3 min via 1A cable with 10cm spatial resolution was converted into

strain and displayed as a 2D contour (Figure 3). In-situ real-time high-resolution strain

profile is useful to visualize in detail a 14-m-long water injection-impacted zone along a

300-m-deep borehole at the Mobara research site, Japan, using different combinations

of instruments and cables. To deeper uncover latent information of optical data, strain

responses should be finely dissected from spatial and temporal scales.

Time series of strain data from the post-processed TW-COTDR measurement at five

depths during water injection test are shown in Figure 3A. Strain histories show strain

variations had a similar pattern having high temporal repeatability. Generally, resulting

strain would be larger in depth closer to the center of injection section. However, strain

@188.6m was less than strain @185.9m, probably owing to formation heterogeneity.

Thus, DFOS tool can concurrently track strain evolution at any point along a FO cable.

Optical data for all depths in MW #1 are shown in Figure 3B to image strain profile. In

order to quantify spatiotemporal strain response, horizontal solid lines provide strain

histories in five depths (Figure 3A) and vertical solid lines depict depth-based strain

profiles in five time points (Figure 3C). As mentioned previously, although there were

lower flowrate short injection (**II** in Figure 2), this stage can be classified into

pre-injection with smaller strain. It is easy to find that large strains were mainly focused

222 on injection section and upper zone within 1 m distance. Due to the presence of fiber

223 clamp and coupling protector (Sun et al., 2020), two strain anomalies occurred in 184.2

224 m and 189.2 m. Besides, based on EMI and resistivity logging in MW, visible strain

225 weakening appeared at silt layers, thus demonstrating that impermeable silts could

226 largely hinder water transport and strain propagation. These observations suggest that

227 inexpensive DFOS has a great future potential to monitor fluid injection-induced

228 geomechanical responses, e.g., wellbore integrity and caprock fracturing in depth.

229
```
Insert Figure 3 here.
```

230 Five depth-dependent strain profiles were selected to analyze nearfield strain evolution

231 (Figure 3C). For injection zone (pink area), induced strain gradually enlarged with time;

232 impacted zone was set within 182.2m~192.3 m (yellow area). Locations of two strain

233 leaps agreed well with those shown in Figure 3B. Therefore, hybrid DFOS is useful to

234 evaluate simultaneously near-wellbore strain evolutions.

235 Water was injected into a 2-m interval across perforation section, migrated along the

236 5.5m-long sand layer, flowed to the fibered well with different patterns resulted from

237 heterogeneous 'arrival' pressures. Pressure fronts of injected water potentially pose

238 different strain footprints logged by DFOS. In analogy with pressure front, strain front is

239 defined in this study. Consequently, strain profile in Figure 2B was normalized based on

240 linear rescaling method to map strain contour with [0, 1] interval (Figure 3D). Unified

241 strain ($N\varepsilon_z^*(t)$) was calculated according to

$$242 \qquad N\varepsilon_z^*(t) = \frac{\varepsilon_z(t) - \varepsilon_z^{\min}}{\varepsilon_z^{\max} - \varepsilon_z^{\min}} \qquad (3)$$

243 where $\varepsilon_z^{\max}$ and $\varepsilon_z^{\min}$ are the maximum and minimum FO strain values. Analogy-

244 based strain fronts were plotted at normalized strains of 0.2 to 1.0 [-]. Note that strain

245 front selection is arbitrary and little effect on the results. Clear-cut strain front allowed

246 highlighting of a C-shaped pattern that has hitherto been not observed. First-arrival

247 interface of each front was located in injection section (black dotted box in Figure3D).

248 Notably, the strain fronts present two obvious fluctuations at 184.2 m and 189.2 m,

249 which are reasonably consistent with previous results (Figures 3B and 3C). Moreover,

250 convergence locations (horizontal white dotted lines in Figure 3D) also exactly matched

251 the range of impacted zone in Figure 3C. It should be noted that there was a dip angle

252 of ~10° between adjacent wells (see Figure 1C), which inevitably contributed to the

253 downward extension of the impacted zone beyond the corresponding injection section.

4. Discussion and Concluding Remarks

255 In this study, an advanced hybrid Brillouin-Rayleigh distributed fiber-optic sensing tool

256 was successfully deployed to in-situ monitor water injection test between two adjacent

257 wells. Testing results showed that DFOS data provided a clear-cut spatiotemporal strain

258 profile along the FO cables in a 300-m-deel well. Our observations demonstrated that

259 injection volume and injection pressure significantly dominated strain magnitude and

260 coverage. Potential injected water-transport footprint and strain impacted zone could

261 be finely visualized via analogy-based strain fronts.

262   Most previous literature utilized DFOS method to monitor near-surface geoengineering

263   (Shanafield et al., 2018). For example, vertical strain changes were sensed via DFOS in

264   the shallow landslide (~15 m) (Kogure & Okuda, 2018) and groundwater pumping site

265   (~145.3 m) (Zhang et al., 2018). By analogy with this water injection, supercritical CO_2

266   injection in deep reservoirs (over 800 m) will pose subsurface-surface strain changes.

267   Therefore, this proven DFOS system can plot the complete strain map, which allows for

268   establish quantitative links between surface deformations with subsurface injections at

269   various future CGS-related geoenergy sites.

270   Lastly, our results subtly quantify cross-well strain data using this proposed hybrid

271   DFOS system, detailed interpret strain evolutions related to injection scenario, mine

272   implied information on fluid transport behaviors. These findings further highlight the

273   wealth of additional detail in spatiotemporal strain dynamics recorded by DFOS and

274   drive future far-field high-resolution crustal imaging applications in geophysics and

275   hydrogeology.

References

Arts, R., & Vandeweijer, V. (2011). The challenges of monitoring CO2 storage. *The Leading Edge*, *30*(9), 1026–1033.

Arts, R., Eiken, O., Chadwick, A., Zweigel, P., van der Meer, L., & Zinszner, B. (2004). Monitoring of CO2 injected at Sleipner using time-lapse seismic data. *Energy*, *29*(9), 1383–1392.

Baatz, R., Bogena, H. R., Franssen Hendricks, H.-J., Huisman, J. A., Montzka, C., & Vereecken, H. (2015). Geomechanics of subsurface water withdrawal and injection. *Water Resources Research*, (51), 5974–5997.

Baldwin, C. S. (2014). Optical fiber sensing in the oil and gas industry: overcoming challenges. In *23rd International Conference on Optical Fiber Sensor* (Vol. 9157, pp. 9157C4-9157–4).

Bao, X., & Chen, L. (2012). Recent Progress in Distributed Fiber Optic Sensors. *Sensors*, *12*(7), 8601–8639.

Bense, V. F., Read, T., Bour, O., Le Borgne, T., Coleman, T., Krause, S., et al. (2016). Distributed Temperature Sensing as a downhole tool in hydrogeology. *Water Resources Research*, *52*(12), 9259–9273.

Chadwick, R. A., Arts, R., Eiken, O., Kirby, G. A., Lindeberg, E., & Zweigel, P. (2004). 4D Seismic Imaging of an Injected CO2 Plume at the Sleipner Field, Central North Sea. In *Petroleum Geology: North-West Europe and Global Perspectives—Proceedings of the 6th Petroleum Geology Conference* (Vol. 29, pp. 311–320).

Ferretti, A., Tamburini, A., Novali, F., Fumagalli, A., Falorni, G., & Rucci, A. (2011). Impact of high resolution radar imagery on reservoir monitoring. *Energy Procedia*, *4*, 3465–3471.

Froggatt, M. E., & Moore, J. (1998). High-spatial-resolution distributed strain measurement in optical fiber with rayleigh scatter. *Applied Optics*, *37*(10), 1735–40.

Jousset, P., Reinsch, T., Ryberg, T., Blanck, H., Clarke, A., Aghayev, R., et al. (2018). Dynamic strain determination using fibre-optic cables allows imaging of seismological and structural features. *Nature Communications*, *9*(1), 2509.

Karegar, M. A., Dixon, T. H., Malservisi, R., Yang, Q., Hossaini, S. A., & Hovorka, S. D. (2015). GPS-based monitoring of surface deformation associated with CO2 injection at an enhanced oil recovery site.

310   *International Journal of Greenhouse Gas Control*, *41*, 116–126.

311   Karrenbach, M., Kahn, D., Cole, S., Ridge, A., Boone, K., Rich, J., et al. (2017).

312   Hydraulic-fracturing-induced strain and microseismic using in situ distributed fiber-optic sensing.

313   In *Leading Edge* (Vol. 36, pp. 837–844). Society of Exploration Geophysicists.

314   Kersey, A. D. (2000). Optical fiber sensors for permanent downwell monitoring applications in the oil and

315   gas industry. *IEICE Transactions on Electronics*, *83*(3), 400–404.

316   Kishida, K., Li, C. H., Nishiguchi, K., Yamauchi, Y., Guzik, A., & Tsuda, T. (2012). Hybrid Brillouin-Rayleigh

317   distributed sensing system. In *SPIE* (Vol. 8421, pp. 84212G-8421–4).

318   Kogure, T., & Okuda, Y. (2018). Monitoring the Vertical Distribution of Rainfall-Induced Strain Changes in

319   a Landslide Measured by Distributed Fiber Optic Sensing With Rayleigh Backscattering.

320   *Geophysical Research Letters*, *45*(9), 4033–4040.

321   Kogure, T., Horiuchi, Y., Kiyama, T., Nishizawa, O., Xue, Z., & Matsuoka, T. (2015). Fiber optic strain

322   measurements using distributed sensor system under static pressure conditions.

323   *BUTSURI-TANSA(Geophysical Exploration)*, *68*(1), 23–38.

324   Lei, X., Xue, Z., & Hashimoto, T. (2019). Fiber Optic Sensing for Geomechanical Monitoring: (2)-

325   Distributed Strain Measurements at a Pumping Test and Geomechanical Modeling of Deformation

326   of Reservoir Rocks. *Applied Sciences*, *9*(3), 417.

327   Lellouch, A., Yuan, S., Spica, Z., Biondi, B., & Ellsworth, W. L. (2019). Seismic Velocity Estimation Using

328   Passive Downhole Distributed Acoustic Sensing Records: Examples From the San Andreas Fault

329   Observatory at Depth. *Journal of Geophysical Research: Solid Earth*, *124*(7), 6931–6948.

330   McColpin, G. R. (2009). Surface Deformation Monitoring As a Cost Effective MMV Method. *Energy*

331   *Procedia*, *1*(1), 2079–2086.

332   Miah, K., & Potter, K. D. (2017). A Review of Hybrid Fiber-Optic Distributed Simultaneous Vibration and

333   Temperature Sensing Technology and Its Geophysical Applications. *Sensors* , *17*(11), 1–25.

334   Murdoch, L. C., Germanovich, L. N., Dewolf, S. J., Moysey, S. M. J., Hanna, A. C., Kim, S., & Duncan, R. G.

335   (2019). Feasibility of using in situ deformation to monitor CO_2 storage. *International Journal of*

336   *Greenhouse Gas Control*, *93*(December), 102853.

337   Nishiguchi, K., Li, C.-H., Guzik, A., & Kishida, K. (2014). Synthetic spectrum approach for Brillouin optical

338   time-domain reflectometry. *Sensors (Basel, Switzerland)*, *14*(3), 4731–4754.

339   Saito, H., Nobuoka, D., Azuma, H., Xue, Z., & Tanase, D. (2006). Time-lapse crosswell seismic tomography

340   for monitoring injected CO2 in an onshore aquifer, Nagaoka, Japan. *Exploration Geophysics*, *37*(1),

341   30–36.

342   Schenato, L. (2017). *A Review of Distributed Fibre Optic Sensors for Geo-Hydrological Applications*.

343   *Applied Sciences*.

344   Shanafield, M., Banks, E. W., Arkwright, J. W., & Hausner, M. B. (2018). Fiber-optic Sensing for

345   Environmental Applications: Where We've Come From- and What's Possible? *Water Resources*

346   *Research*.

347   Siriwardane, H. J., Gondle, R. K., & Bromhal, G. S. (2013). Coupled flow and deformation modeling of

348   carbon dioxide migration in the presence of a caprock fracture during injection. *Energy and Fuels*,

349   *27*(8), 4232–4243.

350   Sun, Y., Xue, Z., & Hashimoto, T. (2018). Fiber optic distributed sensing technology for real-time

351   monitoring water jet tests: Implications for wellbore integrity diagnostics. *Journal of Natural Gas*

352   *Science and Engineering*, *58*, 241–250.

353   Sun, Y., Xue, Z., Hashimoto, T., Lei, X., & Zhang, Y. (2020). Distributed Fiber Optic Sensing System for

354   Well-Based Monitoring Water Injection Tests—A Geomechanical Responses Perspective. *Water*

355   *Resources Research*, *56*(1), e2019WR024794.

356   Vasco, D. W., Rucci, A., Ferretti, A., Novali, F., Bissell, R. C., Ringrose, P. S., et al. (2010). Satellite-based

357   measurements of surface deformation reveal fluid flow associated with the geological storage of

358   carbon dioxide. *Geophysical Research Letters*, *37*(3), 1–5.

359   Verdon, J. P., Kendall, J.-M., Stork, A. L., Chadwick, R. A., White, D. J., & Bissell, R. C. (2013). Comparison

360   of geomechanical deformation induced by megatonne-scale CO2 storage at Sleipner, Weyburn,

361   Verdon, J. P., Stork, A. L., Bissell, R. C., Bond, C. E., & Werner, M. J. (2015). Simulation of seismic events

362   induced by CO2 injection at In Salah , Algeria. *Earth and Planetary Science Letters*, *426*, 118–129.

363   White, J. A., Chiaramonte, L., Ezzedine, S., Foxall, W., Hao, Y., Ramirez, A., & McNab, W. (2014).

364   Geomechanical behavior of the reservoir and caprock system at the In Salah CO2 storage project.

365   *Proceedings of the National Academy of Sciences*, *111*(24), 8747–8752.

366　Wu, Q., Nair, S., Shuck, M., Oort, E. van, Guzik, A., & Kishida, K. (2016). Advanced Distributed Fiber Optic

367　　　Sensors for Monitoring Poor Zonal Isolation with Hydrocarbon Migration in Cemented Annuli.

368　　　*Society of Petroleum Engineers*.

369　Xue, Z., Shi, J.-Q., Yamauchi, Y., & Durucan, S. (2018). Fiber Optic Sensing for Geomechanical Monitoring:

370　　　(1)-Distributed Strain Measurements of Two Sandstones under Hydrostatic Confining and Pore

371　　　Pressure Conditions. *Applied Sciences*, *8*(11), 2103.

372　Zhang, C.-C., Shi, B., Gu, K., Liu, S.-P., Wu, J.-H., Zhang, S., et al. (2018). Vertically Distributed Sensing of

373　　　Deformation Using Fiber Optic Sensing. *Geophysical Research Letters*, *45*(21), 11,711-732,741.

374　Zhang, Y., & Xue, Z. (2019). Deformation-Based Monitoring of Water Migration in Rocks Using

375　　　Distributed Fiber Optic Strain Sensing: A Laboratory Study. *Water Resources Research*, (55).

376　Zhang, Y., Xue, Z., Park, H., Shi, J. Q., Kiyama, T., Lei, X., et al. (2019). Tracking CO2 plumes in clay-rich

377　　　rock by distributed fiber optic strain sensing (DFOSS): a laboratory demonstration. *Water*

378　　　*Resources Research*, (55), 856–867.

379　Zoback, M. D., & Gorelick, S. M. (2012). Earthquake triggering and large-scale geologic storage of carbon

380　　　dioxide. *Proceedings of the National Academy of Sciences* , *109*(26), 10164–10168.

381

382

383

384

385

386

387

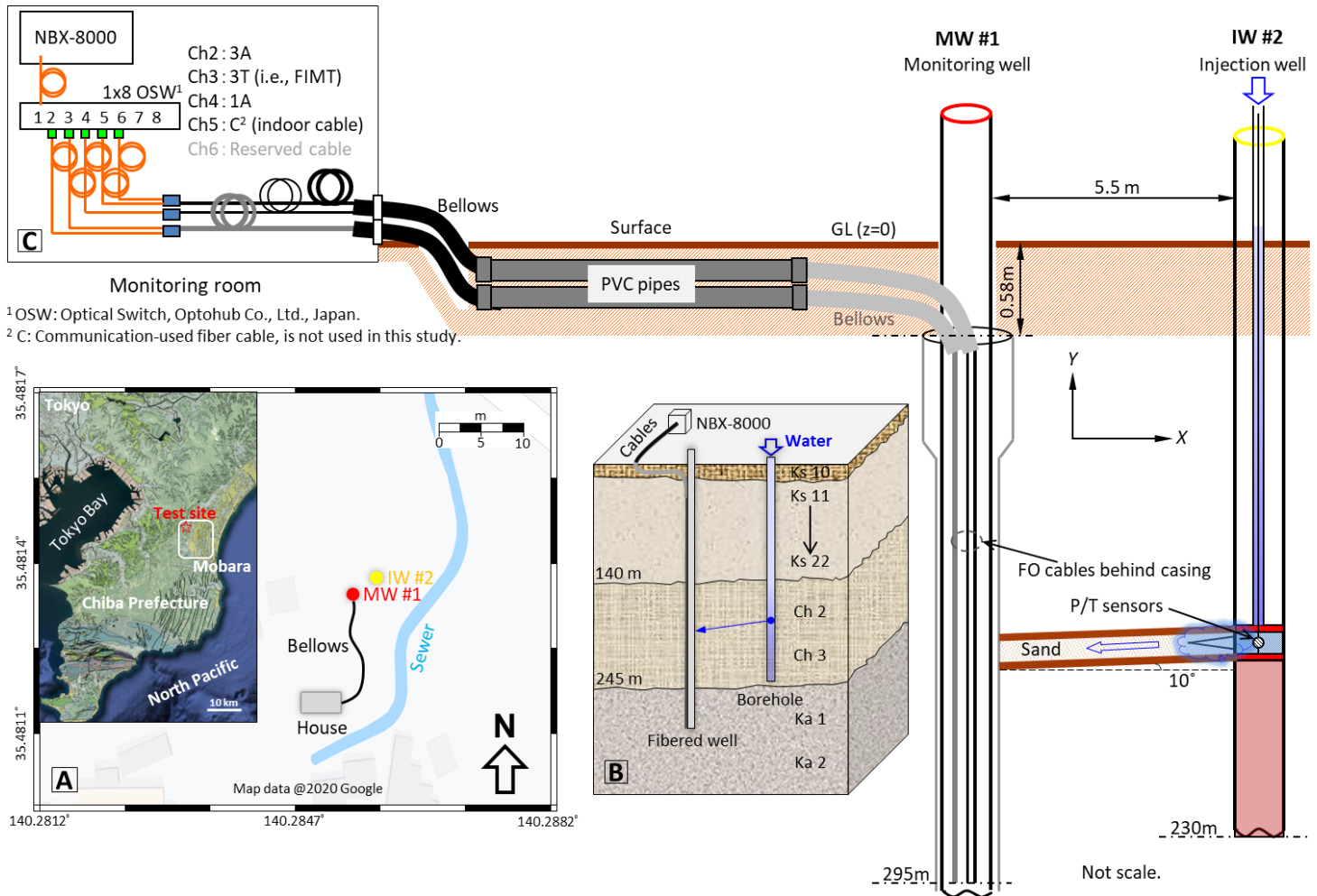388

389

390

391

392

393

Figures

395 **Figure 1.** Field site and FO cables layout. (**A**) Map of water injection test. Inset depicts the location

396 of Mobara-shi, Chiba Prefecture, Central Japan (white box) and test site (red star). Red and yellow

397 circles denote monitoring well (MW #1) and injection well (IW #2). (**B**) 3D view of two adjacent

398 wells configuration and local stratigraphy. (**C**) Schematic illustration showing three whole-length

399 single-ended FO cables deployment and borehole geometry. Based on geophysical logging, dip

400 angle is about 10˚ for the injection formation. Note that 5.5 m is interwell distance at the surface.
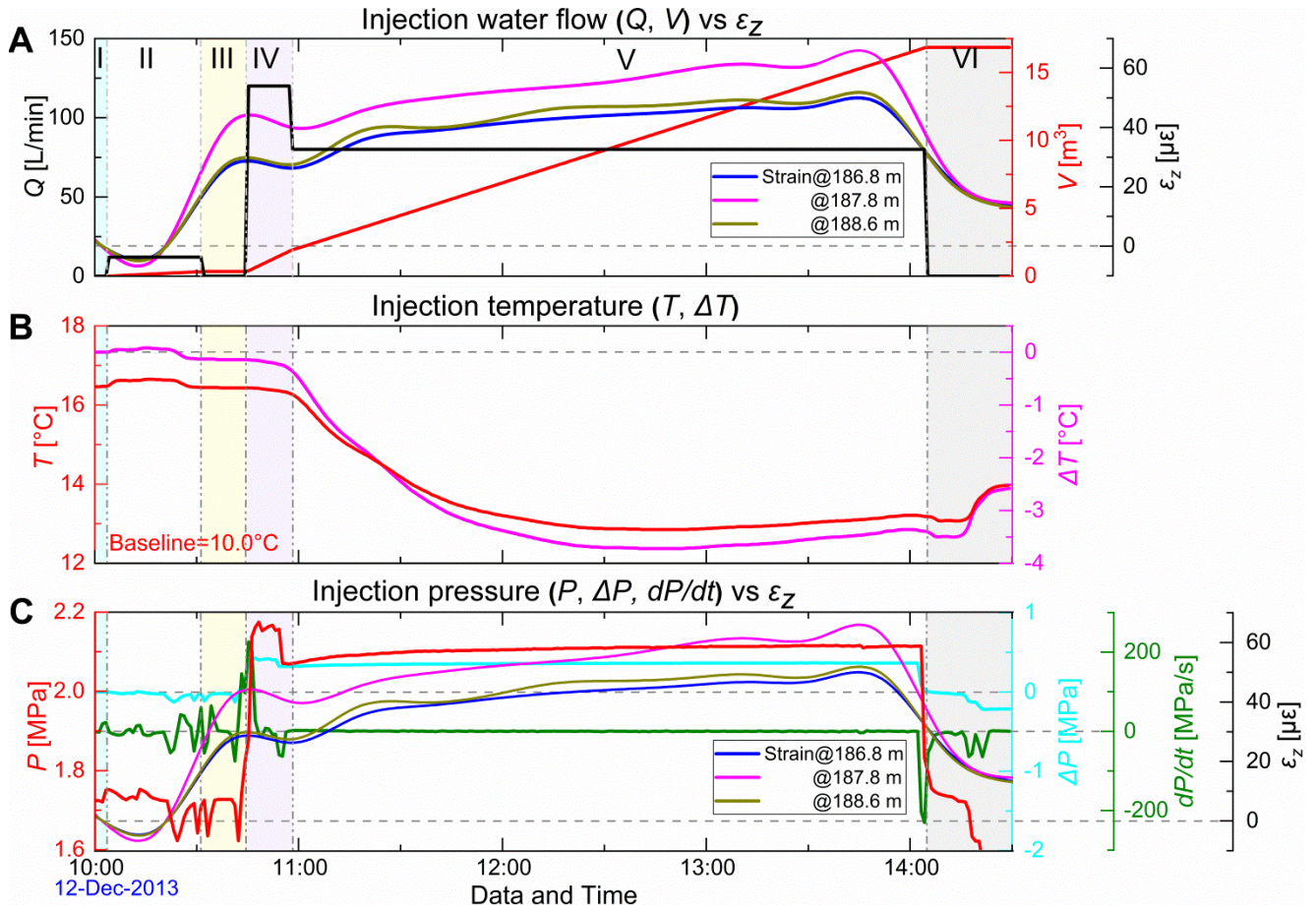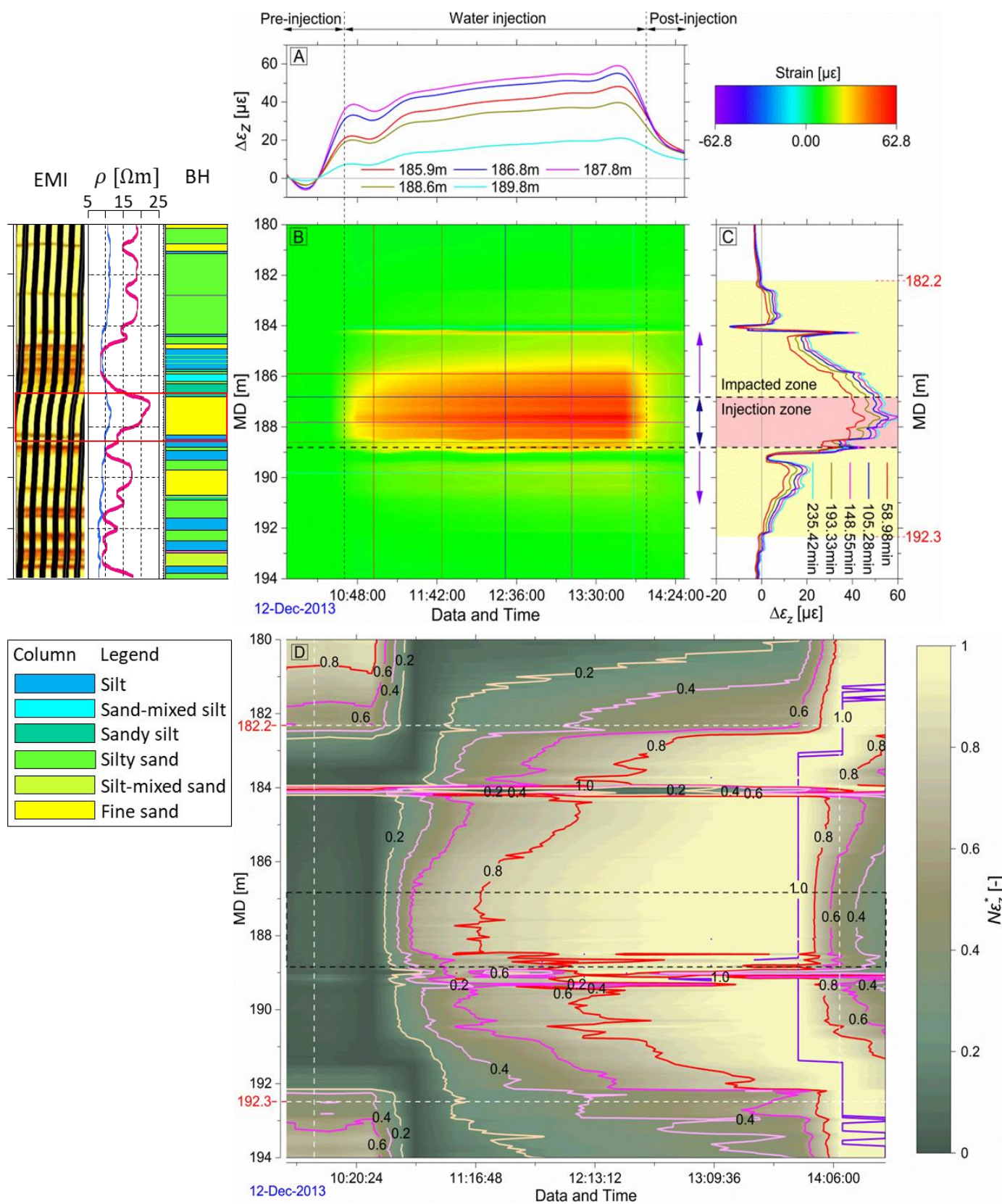
Figure 2. Multi-parameter observations of time-lapse water injection scenario with induced strains.

(**A**) Injection water flow reanalysis of IW #2-wellhead flowmeter data, injection rate Q (black) and

cumulative volume V =Q·t (red) show six injection stages (**I** to **VI**, marked with dashed vertical lines)

with strain profiles monitored at the depths of 186.8 m (blue), 187.8 m (magenta) and 188.6 m

(dark yellow), respectively in MW #1. (**B**) Temperature log of injected water recorded by built-in T

sensor near the injection ports in IW #2 (see Figure 1C) and corresponding temperature variation

(pink). Water temperature in the tank is about 10.0℃. (**C**) Injection pressure P (red), pressure

change ΔP (cyan) and pressure gradient dP/dt (olive) with three strain profiles, same as (A).

Pressure increment $\Delta P = P_t - P_0$.

Figure 3. Spatiotemporal strain responses during the injection test and corresponding normalized

411 strain profile. (**A**) Time-varying strain histories at depths of 185.9 m (red), 186.8 m (blue), 187.8 m

412 (magenta), 188.6 m (dark yellow) and 189.8m (cyan), respectively. (**B**) Time-depth induced strain

413 image mapped with Rayleigh fiber-optic sensing recordings. Electrical micro imager (EMI) shows a

414 laminated sand/shale sequence of the formations in MW #1, generally brighter yellow colors for

415 more resistive sand-rich facies while darker brown colors for less resistive shale–rich facies. ρ:

416 electrical resistivity in formation. Borehole histogram (BH) is plotted based on EMI and resistivity

417 logs. Red solid box and black dotted lines denote injection section. (**C**) Depth-dependent strain

418 profiles at five injection time points of 58.98 min (red), 105.28 min (blue), 148.55 min (magenta),

419 193.33 min (dark yellow) and 235.42 min (cyan). Impacted zone is marked with yellow boxes. 182.8

420 m and 192.3 m are the critical depths of impacted zone. (**D**) Normalized strain profiles and

421 analogy-based strain fronts. Normalized strain contour lines of 0.2 (light yellow), 0.4 (light pink), 0.6

422 (pink), 0.8 (red) and 1.0 (violet) contour lines are plotted to exhibit potential strain fronts. Black

423 dotted box denotes injection section, and horizontal dotted lines are the convergence depths.

Figure 1.

NBX-8000

Ch2 : 3A
Ch3 : 3T (i.e., FIMT)
Ch4 : 1A
Ch5 : C[2] (indoor cable)
Ch6 : Reserved cable

1x8 OSW[1]
1 2 3 4 5 6 7 8

C

Monitoring room

[1] OSW: Optical Switch, Optohub Co., Ltd., Japan.
[2] C: Communication-used fiber cable, is not used in this study.

Bellows

Surface

GL (z=0)

PVC pipes

Bellows

MW #1
Monitoring well

IW #2
Injection well

5.5 m

0.58m

Y

X

FO cables behind casing

P/T sensors

Sand

10°

230m

295m

Not scale.

A

Tokyo

Tokyo Bay

Test site

Mobara

Chiba Prefecture

North Pacific

10 km

m
0   5   10

IW #2

MW #1

Bellows

Sewer

House

N

Map data @2020 Google

35.4817°

35.4814°

35.4811°

140.2812°   140.2847°   140.2882°

B

Cables   NBX-8000

Water

Ks 10

Ks 11

Ks 22

140 m

245 m

Ch 2

Ch 3

Borehole
Ka 1

Ka 2

Fibered well

Figure 2.

A — Injection water flow (*Q*, *V*) vs ε_z

I II III IV V VI

Q [L/min] — V [m³] — ε_z [με]

- Strain@186.8 m
- @187.8 m
- @188.6 m

B — Injection temperature (*T*, ΔT)

T [°C] — ΔT [°C]

Baseline=10.0°C

C — Injection pressure (*P*, ΔP, *dP/dt*) vs ε_z

P [MPa] — ΔP [MPa] — dP/dt [MPa/s] — ε_z [με]

- Strain@186.8 m
- @187.8 m
- @188.6 m

12-Dec-2013

Data and Time

Figure 3.